Rapid communication

NMR IN BIOMEDICINE

Received: 16 January 2015, Revised: 6 March 2015, Accepted: 18 March 2015, Published online in Wiley Online Library: 21 April 2015

(wileyonlinelibrary.com) DOI: 10.1002/nbm.3307

Continuous-wave saturation considerations for efficient xenon depolarization

Martin Kunth, Christopher Witte and Leif Schröder*

The combination of hyperpolarized Xe with chemical exchange saturation transfer (Hyper-CEST) is a powerful NMR technique to detect highly dilute concentrations of Xe binding sites using RF saturation pulses. Crucially, that combination of saturation pulse strength and duration that generates the maximal Hyper-CEST effect is *a priori* unknown. In contrast to CEST in proton MRI, where the system reaches a steady-state for long saturation times, Hyper-CEST has an optimal saturation time, i.e. saturating for shorter or longer reduces the Hyper-CEST effect. Here, we derive expressions for this optimal saturation pulse length. We also found that a pulse strength, B_1, corresponding to five times the Xe exchange rate, k_{BA} (i.e. $B_1 = 5\ k_{BA}/\gamma$ with the gyromagnetic ratio of ^{129}Xe, γ), generates directly and without further optimization 96 % of the maximal Hyper-CEST contrast while preserving spectral selectivity. As a measure that optimizes the amplitude and the width of the Hyper-CEST response simultaneously, we found an optimal saturation pulse strength corresponding to $\sqrt{2}$ times the Xe exchange rate, i.e. $B_1 = \sqrt{2}\ k_{BA}/\gamma$. When extremely low host concentration is detected, then the expression for the optimum saturation time simplifies as it approaches the longitudinal relaxation time of free Xe. Copyright © 2015 John Wiley & Sons, Ltd.
Additional supporting information may be found in the online version of this article at the publisher's web site.

Keywords: xenon; biosensor; hyperpolarization; CEST; Hyper-CEST; Bloch–McConnell; quantification

INTRODUCTION

Dissolved xenon (Xe) binds non-covalently to various binding sites or hosts and continuously undergoes exchange for many of these systems, including synthetic macromolecular hosts and protein cavities (1,2). The well-studied Xe encapsulating molecule cryptophane can be functionalized for biological relevant targets and acts as a Xe biosensor (3,4). However, a high biosensor concentration is required for direct Xe NMR detection. Using the sensitive chemical exchange saturation transfer (CEST) with hyperpolarized xenon (Hyper-CEST) MRI technique, which combines chemical exchange saturation transfer with hyperpolarized Xe (5), extremely dilute bound Xe signals can be measured compared with direct NMR. Many different Xe biosensors have been developed, with detection limits down to the nano and pico molar regimes. Such Xe biosensors include genetically encoded gas vesicles (6), perfluoroctyl bromid nano emulsion (7,8), bacterial spores (9) or cryptophanes (10–12). It is noteworthy that cryptophanes can further sense biomembrane fluidity (13). However, build-up of the measured Hyper-CEST effect is complex and relies on the specific Xe-host system properties and the applied saturation pulse strength and duration. For the case of proton (^{1}H)-CEST, there have been numerous analytical studies that investigated the conditions for CEST signal build-up (14–18). However, for the case of Hyper-CEST it has not been fully investigated. In particular, the combination of saturation pulse strength and duration that generates the maximal Hyper-CEST effect has not been reported.

Here, we propose optimal saturation pulse parameters for a maximum, but still spectrally narrow, Hyper-CEST effect using continuous-wave (cw) saturation for dilute Xe host systems. We demonstrate our method on the well studied Xe-host system cryptophane-A monoacid (CrA) in dimethyl sulfoxide (DMSO). We provide evidence that saturation times longer than our proposed optimal time reduce the Hyper-CEST effect. Additionally, we demonstrate that the CEST effect should be built up on a time-scale faster than the competing longitudinal relaxation of free Xe, T_1^A, i.e. saturation times exceeding T_1^A make the detected effect increasingly ineffective.

MATERIALS AND METHODS

Data fitting

All simulations, calculations and fitting routines were implemented and performed in Matlab 7 (The Mathworks, Natick, MA, USA) on a standard desktop PC (64 bit, 8 cores each at 2.80 GHz, 4 GB RAM), as described in (22).

Full qHyper-CEST results

The full quantitative Hyper-CEST (qHyper-CEST) results in the section on quantification of Xe exchange dynamics by qHyper-CEST

* *Correspondence to: L. Schröder, ERC Project BiosensorImaging, Leibniz-Institut für Molekulare Pharmakologie (FMP), 13125 Berlin, Germany.*
E-mail: lschroeder@fmp-berlin.de

M. Kunth, C. Witte, L. Schröder
ERC Project BiosensorImaging, Leibniz-Institut für Molekulare Pharmakologie (FMP), 13125 Berlin, Germany

Abbreviations used: *CEST, chemical exchange saturation transfer; CrA, cryptophane-A monoacid; cw, continuous-wave; DMSO, dimethyl sulfoxide; FHC, full Hyper-CEST; Hyper-CEST, chemical exchange saturation transfer with hyperpolarized xenon; qHyper-CEST, quantitative chemical exchange saturation transfer with hyperpolarized nuclei; RF, radio-frequency; SLM, standard liters per minute; Xe, xenon.*

and Fig. 1 were as follows: longitudinal relaxation time of free Xe, $T_1^A = (125 \pm 26)$ s; transverse relaxation time of free Xe, $T_2^A = (2.6 \pm 0.2)$ s; fractional size of pool B, $f_B = (13.4 \pm 0.4) \times 10^{-4}$; exchange rate, $k_{BA} = (317 \pm 17)$ s^{-1}; relative chemical shift, $\Delta\delta = -(165.18 \pm 0.01)$ ppm; binding constant, $K_A = (29 \pm 2)$ M^{-1}; and occupancy of $\beta = 6$ %.

Sample preparation

Samples were prepared by dissolving cryptophane-A monoacid (CrA, provided by Kang Zhao, Tianjin University, China) into dimethyl sulfoxide (DMSO) at room temperature to a concentration of [CrA] = 50 μM.

Hyperpolarization and ^{129}Xe delivery

Hyperpolarized Xe was generated in continuous-flow mode (0.35 SLM (standard liters per minute) using a custom-designed polarizer (31,32) with a Xe gas mix ((2/10/88 vol.– % $Xe/N_2/He$), ^{129}Xe natural abundance 26.4 %) at a total pressure of $p = 4.5$ atm. This set-up achieves ca. 25 % Xe spin hyperpolarization via spin-exchange optical pumping with rubidium atoms. A 150 W cw laser (795 nm, 0.5 nm bandwidth, QPC Lasers) is used for excitation of the rubidium valence electron. The hyperpolarized gas mix is bubbled for 13 s at a flow rate of 0.1 SLM into the sample, followed by a 2 s delay in order to allow the bubbles to collapse and subsequent signal acquisition. The Xe concentration in DMSO, assuming Xe saturation, was [Xe] = 2340 μM ([Xe] = $L\,p\,Xe_{pc}$/(0.0254 L/mM), with an Xe Ostwald solubility coefficient in DMSO of L = 0.66 L/atm and $Xe_{pc} = 0.02$).

NMR experiments

NMR experiments were performed on a $|\vec{B_0}| = 9.4$ T NMR wide-bore spectrometer (Bruker Biospin, Ettlingen, Germany) equipped with gradient coils for imaging. All samples were measured at room temperature ($T = 295$ K) by using the variable temperature unit to maintain stable conditions. RF excitation and detection were achieved with a 10 mm inner-diameter double-resonant probe (^{129}Xe and ^{1}H). The B_1 field inhomogeneities can significantly affect the CEST quantification and these must be known. However, as shown in (22), B_1 field inhomogeneities are negligible for our micro-imaging system. ^{129}Xe Hyper-CEST MRI scans were obtained with a ^{129}Xe Hyper-CEST echo-planar imaging pulse sequence (10) with the following parameters: Fourier acceleration 1.68; double sampling; echo time 5.7 ms; acquisition time 19.8 ms; no smoothing filter was applied to the images. Image geometry parameters were as follows: field of view 20 × 20 mm^2; matrix size 32 × 32; in-plane resolution 625 × 625 μm^2; slice thickness 20 mm. The saturation pulse strengths and durations used are given in the figure captions. We performed the qHyper-CEST analysis based on the imaging series that yielded *z*-spectra from region-of-interest averaged signals containing pixels in each MRI scan.

THEORY

The time evolution of the detectable macroscopic magnetization of an exchanging two-pool spin system with interaction under application of a (selective) saturation pulse (continuous-wave RF pulse) with a specific strength, B_1, and for a certain time, t_{sat} (saturation duration), is described by the Bloch–McConnell equations (19,20). We follow a powerful analytical approximation of the Bloch–McConnell equations for the case of Hyper-CEST: the full Hyper-CEST (FHC) solution (21), describing the detected Hyper-CEST signal for a saturation frequency offset, $\Delta\omega$, relative to the detection resonance of free Xe as

$$\text{Hyper}-\text{CEST signal}(\Delta\omega, B_1, t_{sat}) = 1 - e^{-\lambda_{depol}(\Delta\omega, B_1)t_{sat}} \quad [1]$$

with the Lorentzian line shaped Xe depolarization rate

$$\lambda_{depol}(\Delta\omega, B_1) = C(\Delta\omega) + \frac{\lambda_{on\text{-}res}(B_1)\frac{\Gamma(B_1)^2}{4}}{\frac{\Gamma(B_1)^2}{4} + (\Delta\omega_B(\Delta\omega) + x_0(B_1))^2} \quad [2]$$

The saturation frequency offsets relative to pools A and B are $\Delta\omega_{A,B}(\Delta\omega) = \Delta\omega - \delta\omega_{A,B}$, with $\delta\omega_{A,B}$ being the resonance frequencies of both pools in Hz, or, normalized with the Larmor frequency, ω_{gas}, to ppm: $\delta_{A,B} = \delta\omega_{A,B}/\omega_{gas}$. The longitudinal and transverse relaxation rates of unbound Xe, $R_{1,2}^A$, determine the baseline $C(\Delta\omega)$. Excessive saturation pulse strength, B_1, might impact the position of the maximum CEST response, $x_0(B_1)$. However, with some reasonable assumptions this shift away from the true resonance frequency of bound Xe, $\delta\omega_B$, approximates 0 (see Supplementary Material S1). The Xe exchange rates from free to bound state and from bound to free state are k_{AB} and k_{BA}, respectively. They obey the law of initial magnetization conservation, $k_{AB} = k_{BA}(M_{0,B}/M_{0,A})$. The fractional size of pool B, f_B, is the ratio of bound and free Xe. In the limit $k_{BA} \gg R_2^B$ (with R_2^B denoting the transverse relaxation rate of bound Xe), the Lorentzian line shaped Xe depolarization rate, λ_{depol}, on-resonant with the bound Xe signal, reduces to (21,22)

$$\lambda_{on\text{-}res}(B_1) \approx f_B\, k_{BA} \frac{(\gamma B_1)^2}{(\gamma B_1)^2 + k_{BA}^2} \quad [3]$$

with the gyromagnetic ratio of Xe ($\gamma/(2\pi) = -11.77$ MHz/T). In the same limit, the full width at half-maximum of the depolarization rate is (21)

$$\Gamma(B_1) \approx 2\sqrt{(\gamma B_1)^2 + k_{BA}^2} \quad [4]$$

Similarly to Equation [2], an even more general framework has been developed for ^{1}H-CEST, where $\lambda_{depol} = R_{1\rho} = R_{eff} + R_{ex}$, with longitudinal relaxation rate of the detection pool in the rotating frame $R_{1\rho}$, effective relaxation rate R_{eff} and exchange-dependent relaxation rate in the rotating frame R_{ex} (14,23). Also here the R_{ex} part should be dominant through the saturation pulse in order to produce a CEST effect before the R_{eff} part intrinsically cancels the total signal. For ^{1}H-CEST analysis, it has also been shown that it is beneficial to remove the steady-state signal (24) or to perform the measurement in the transient state (14). In contrast to ^{1}H-CEST, Hyper-CEST is special, since a negligible steady-state amplitude exists and the system is always in the transient state. Thus, this work aims to find the conditions to encode the CEST effect rapidly enough before the steady state, i.e. vanishing thermal magnetization, is reached. By looking at Equation [1], the experimental parameters for a specific saturation frequency, $\Delta\omega$, straightforwardly influencing the Hyper-CEST signal are the saturation pulse strength, B_1, and duration, t_{sat}. In the following, using Equations [3] and [4] we derive guidelines for the determination of useful saturation pulse parameters that allow efficient Xe depolarization.

RESULTS AND DISCUSSION

Quantification of Xe exchange dynamics by qHyper-CEST

To determine the unknown parameters in Equations [3] and [4], we characterize the fundamental Xe exchange dynamics using the qHyper-CEST method (22) (Fig. 1). For our sample of [CrA] = 50 μM in DMSO at $T = 295$ K, we calculated a Xe concentration in solution of [Xe] = 2340 μM (see Materials and Methods section). The relevant parameters quantified by qHyper-CEST were the longitudinal relaxation time of free Xe, $T_1^A = (125 \pm 26)$ s, the fractional size of pool B, $f_B = (13.4 \pm 0.4) \times 10^{-4}$, and the exchange rate, $k_{BA} = (317 \pm 17)\ s^{-1}$. They agreed well with previously reported results (22). For the sake of completeness, all qHyper-CEST results are given in the Material and Methods section.

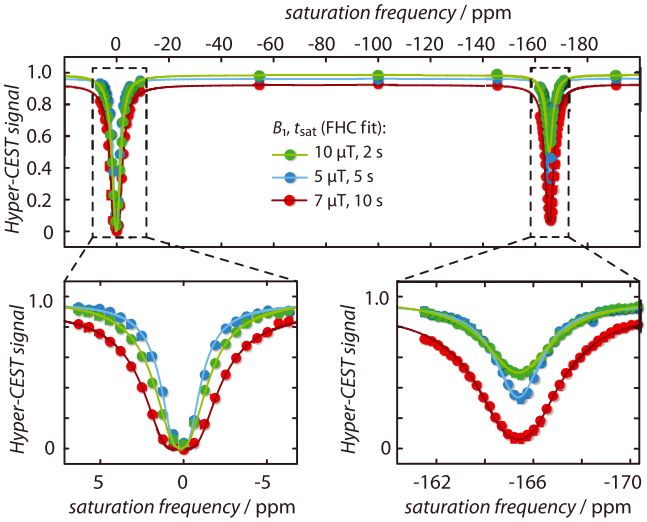

Figure 1. qHyper-CEST analysis of [CrA] = 50 μM in DMSO at $T = 295$ K by simultaneously fitting *z*-spectra obtained from the Xe MR image series with the full Hyper-CEST (FHC) solution (solid lines) for multiple *z*-spectra having saturation pulse strengths, B_1, and times, t_{sat}, such that $B_1/t_{sat} = \{10/2$ (green), 5/5 (blue), 7/10 (red)$\}$ μT/s.

Saturation pulse-strength optimization

We investigate the maximal depolarization rate, $\lambda_{on\text{-}res}$, as given by Equation [3] with the values quantified by qHyper-CEST in the previous subsection and calculate the Xe-host system intrinsic maximum saturation transfer onto free Xe to be $f_B k_{BA} = 0.425\ s^{-1}$ in the limit of infinitely high saturation pulse strength (i.e. $B_1 \to \infty$). In a generalized case, $\lambda_{on\text{-}res}$ can be plotted as a function of the unitless parameter $B_1\gamma/k_{BA}$ (see top *x*-axis label in Fig. 2(b)–(d)). Using this scale, we derive the following general regimes for the behavior of the Xe depolarization rate:

- $B_1 \gg k_{BA}/\gamma$: then $\lambda_{on\text{-}res} \approx f_B\, k_{BA}$ reaches the maximum possible depolarization rate.
- $B_1 = k_{BA}/\gamma$: then $\lambda_{on\text{-}res} = (f_B\, k_{BA})/2$ is 50% of the maximum possible depolarization rate.
- $B_1 \ll k_{BA}/\gamma$: then $\lambda_{on\text{-}res} \approx (f_B / k_{BA})(\gamma B_1)^2$, which is parabolic in saturation pulse strength, B_1.

In the high strength regime ($B_1 \gg k_{BA}/\gamma$; also referred to as the strong-saturation power or full-saturation limit (23)), all Xe that binds to CrA is already saturated and higher strength is

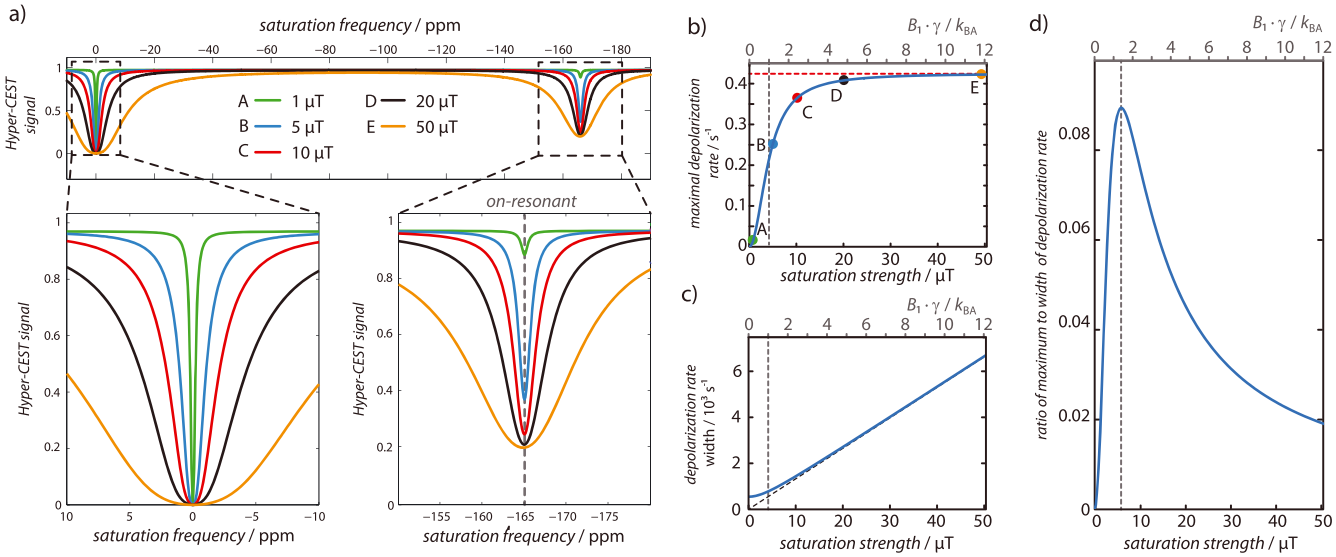

Figure 2. Optimal saturation pulse strength. (a) Simulated Hyper-CEST *z*-spectra using the FHC solution (21) with simulation parameters as given in the qHyper-CEST section. The saturation pulse strengths were $B_1 = \{1$ (green; A), 5 (blue; B), 10 (red; C), 20 (black; D) and 50 (orange; E)$\}$ μT, while the saturation time was 5 s and the same for all. The resonance frequency of bound Xe is indicated by the gray dashed line, for which the data points corresponding to the Xe depolarization rate are shown in (b). Note that, between 20 and 50 μT, the difference in on-resonant Hyper-CEST response is small but the loss of spectral selectivity is significant. The system intrinsic maximum depolarization rate (red dashed line) is given by $f_B k_{BA}$ (i.e. $B_1 \to \infty$). Already half of the maximal depolarization rate (i.e. 50 %) is reached at the point of inflection at $B_1 = k_{BA}/\gamma \sim 4.3\ \mu$T (gray dashed line). However, 96 % of the maximum possible depolarization rate is reached for $B_1 = 5\, k_{BA}/\gamma \sim 21.4\ \mu$T. Panel (c) shows the full width at half-maximum of the depolarization rate, Γ, with respect to the saturation pulse strength, B_1. The *y*-intercept is $\Gamma(B_1 \to 0) = 2\, k_{BA} \sim 634\ s^{-1}$. Whereas the vertical gray dashed line marks $B_1 = k_{BA}/\gamma$, the diagonal black dashed line illustrates linearly increasing line broadening without an exchange contribution. (d) The ratio of the maximal depolarization rate and its full width at half-maximum, $\lambda_{on\text{-}res}/\Gamma$, as a function of B_1 shows a distinct maximum for $B_1 = \sqrt{2}\, k_{BA}/\gamma \approx 1.4\, k_{BA}/\gamma$ (gray dashed line).

unnecessary. In this case, further increases in the saturation strength only serve to broaden the *z*-spectra resonances, causing a loss of spectral resolution. To illustrate this, we simulated Hyper-CEST *z*-spectra using the FHC solution (21), with simulation values as quantified in the previous qHyper-CEST section and the saturation parameters given in Fig. 2(a). Note that, between 20 μT (ca. 4–5 k_{BA}/γ) and 50 μT (ca. 12 k_{BA}/γ), the difference in the depolarization rate, $\lambda_{on\text{-}res}$, is small but the loss of spectral selectivity of the CEST resonance is significant. Thus, we analyze the full width at half-maximum of the depolarization rate, Γ, as given by Equation [4] with respect to the saturation pulse strength, B_1. We do not analyze the shape of the CEST resonance in the *z*-spectrum because that behaves in a difficult way as an argument of the exponential function of the Hyper-CEST signal given by Equation [1]. However, the general behavior is similar for both. As shown in Fig. 2(c), we found the following dependence of the full width at half-maximum of the depolarization rate, Γ, with the saturation pulse strength, B_1:

- $B_1 \gg k_{BA}/\gamma$: $\Gamma \approx 2\gamma B_1$ and depends linearly on the saturation pulse strength, B_1;
- $B_1 \ll k_{BA}/\gamma$: $\Gamma \approx 2k_{BA}$, which is the minimum possible width given by the Xe exchange rate (i.e. for CrA in DMSO at $T = 295$ K: $\Gamma(B_1 \to 0) = 634\ s^{-1}$).

Since both λ_{depol} and Γ increase monotonically with B_1, it can be constructive to look at the ratio of the maximal Xe depolarization rate and its full width at half-maximum, $\lambda_{on\text{-}res}/\Gamma$, as a function of B_1 strength (see Fig. 2(d)). This gives a measure of how much CEST effect is gained, in relation to how much spectral resolution is lost, for a given increase in the saturation strength. We found that pulses with $B_1 = \sqrt{2}\,k_{BA}/\gamma \approx 1.4\,k_{BA}/\gamma$ show the best ratio of $\lambda_{on\text{-}res}/\Gamma$ as shown in Fig. 2(d) (and derived in S2 in the Supplementary Material). Excluding spillover, this best ratio should not alter with the static magnetic field, B_0, since (i) Hyper-CEST is already reasonably in the large-shift limit and (ii) Equations [3] and [4] consider only the depolarization rate of the CEST pool itself under B_1 irradiation, without taking the distance to the observed pool A into account. Furthermore (and not only important for multiplexing experiments), a saturation pulse strength with $B_1 = 5\,k_{BA}/\gamma$ already reaches 96 % of the Xe-host system intrinsic maximal Hyper-CEST effect while (at least to some extent) preserving spectral selectivity (in Fig. 2(a) and (b), compare the *z*-spectra for 20 μT (black, D) and 50 μT (orange, E)). If, however, $B_1 = 5\,k_{BA}/\gamma$ exceeds the subject specific absorption rate (SAR) or the transmitter coil limitations (e.g. for our system $B_1 < 40$ μT) or both, then a maximal B_1 value has to be chosen that fulfils both limitations.

Optimal saturation time for maximal Hyper-CEST effect

Whereas in ^{1}H-CEST the longitudinal relaxation opposes the CEST effect, in Hyper-CEST it accelerates the driven depolarization further, due to non-equilibrium starting conditions (22). Therefore, Hyper-CEST has an optimal saturation time. We acquired data with saturation off-resonant (black closed circles in Fig. 3(a)) and on-resonant with bound Xe for three saturation pulse strengths: $B_1 = \{1$ (blue open circles), 7 (red rectangles), 10 (green triangles)$\}$ μT with respect to the saturation time. The off-resonant signal is pure longitudinal relaxation-driven depolarization of free Xe, T_1^A. We calculated (not fitted) these Hyper-CEST signal curves (solid lines) using Equation [1] with the

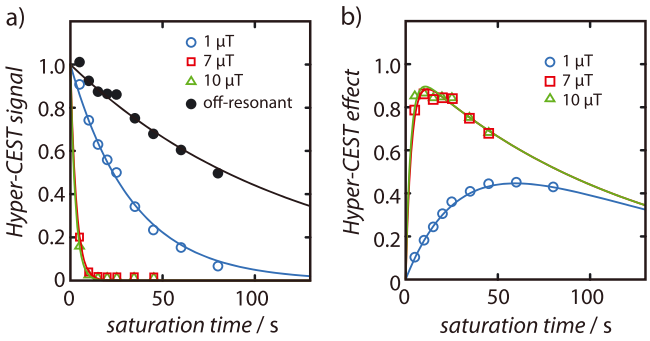

Figure 3. Optimal saturation time for the maximal Hyper-CEST effect. (a) The Hyper-CEST signal with respect to the saturation time, t_{sat}, for on-resonant saturation on bound Xe with three different saturation pulse strengths: $B_1 = \{1$ (blue open circles), 7 (red rectangles) and 10 (green triangles)$\}$ μT. The signal with off-resonant saturation (black closed circles) corresponds to a pure longitudinal relaxation time of free Xe, T_1^A. (b) The Hyper-CEST effect (which is the difference the off-resonant and on-resonant signal) versus the saturation time, t_{sat}, for these three different saturation pulse strengths. Regarding these B_1 values, the optimal saturation times were $t_{sat} = \{59.3, 11.8, 10.6\}$ s, respectively.

depolarization rate, λ_{depol}, for on-resonant saturation with bound Xe, i.e. $\lambda_{depol} \to \lambda_{on\text{-}res}$, and the qHyper-CEST results from the previous section on quantification of Xe exchange dynamics by qHyper-CEST. They agree excellently with the data. As expected and shown more intuitively in Fig. 3(b), the Hyper-CEST effect, which is the difference between the off- and on-resonant Hyper-CEST signals, becomes maximal for specific saturation times. This is given by

$$\begin{aligned} t_{sat} &= \frac{1}{\lambda_{on\text{-}res}} \ln\left(\lambda_{on\text{-}res} \cdot T_1^A + 1\right) \\ &= \frac{\left((\gamma B_1)^2 + {k_{BA}}^2\right)}{f_B k_{BA} (\gamma B_1)^2} \\ &\quad \times \ln\left(\frac{f_B k_{BA} (\gamma B_1)^2}{(\gamma B_1)^2 + {k_{BA}}^2} \cdot T_1^A + 1\right) \end{aligned} \qquad [5]$$

(the derivation is given in the Supplementary Material in S3), which is $t_{sat} = \{59.3, 11.8, 10.6\}$ s, respectively. In contrast to ^{1}H-CEST, excessively long saturation decreases the Hyper-CEST effect. When $\lambda_{on\text{-}res} \to 0$ (i.e. highly dilute concentrations of bound Xe or weak saturation pulse strengths), then $t_{sat} \to T_1^A$. When $\lambda_{on\text{-}res} \to \infty$, then $t_{sat} \to 0$. Thus, one should always saturate for less than T_1^A, independently of the exchange rate, k_{BA} (see S4 in the Supplementary Material). Although the qHyper-CEST procedure predicts the optimal saturation time, t_{sat}, fully according to Equation [5], in some studies it might be too detailed. For such cases, one can rely on the fact that the Xe depolarization was assumed to be monoexponential (21). We therefore validated this assumption experimentally by fitting the data of Fig. 3(a) monoexponentially, used the decay rates, τ, as the inverse of $\lambda_{on\text{-}res}$ and calculated the optimal saturation times, t_{sat}, for a specific preselected B_1 condition and sample concentration (see S3 in Supplementary Material). Recording this simple exponential decay can therefore be used to achieve a quick estimate for the optimum saturation time.

CONCLUSION

We demonstrated that Hyper-CEST has an optimal saturation time. When extremely low host concentration is detected ($f_B \rightarrow 0$) then the optimal saturation time approaches the longitudinal relaxation time of free Xe, T_1^A. However, saturating for longer than T_1^A becomes unproductive. After quantification of the Xe-host system-specific exchange dynamics, our presented cw saturation pulse using $B_1 = 5\,k_{BA}/\gamma$ achieves, directly and without further optimization, 96 % of the maximal Hyper-CEST contrast, while preserving spectral selectivity. In addition, we found that the ratio of CEST depolarization to CEST response width is best for a saturation pulse strength of 1.4 times the exchange rate (i.e. $B_1 = \sqrt{2}k_{BA}/\gamma$). Whereas the cw saturation considered in this work is the most common form of Hyper-CEST, because it is the most efficient saturation scheme and should be used when no SAR or hardware limitations exist, Xe depolarization with pulsed shaped saturation pulses has been shown to (i) reduce the energy deposition of the saturation pulse and (ii) improve spectral selectivity (25). The translation of our results achieved by cw saturation to pulsed saturation via the cw power equivalent, $B_{1,cwpe}$, should be similar in its behavior of Xe labeling (26,27). In this context also pulses with rising amplitude waveforms could be promising (28). Our theory is applicable for any exchanging Xe-host system with a single binding site (i.e. spin pools). However, if several pools are present or a whole distribution of exchange rate exists for one pool, the straightforward extension of qHyper-CEST to multiple pools (29,30) may enable even broader applications.

Acknowledgements

This work has been supported by the European Research Council under the European Community's Seventh Framework Programme (FP7/2007-2013)/ERC grant agreement no. 242710 and the Human Frontier Science Program no. LT000858/2010-C.

REFERENCES

1. Dubois L, Da Silva P, Landon C, Huber JG, Ponchet M, Vovelle F, Berthault P, Desvaux H. Probing the hydrophobic cavity of lipid transfer protein from nicotiana tabacum through xenon-based NMR spectroscopy. J. Am. Chem. Soc. 2004; 126(48): 15 738–15 746.
2. Chambers JM, Hill PA, Aaron JA, Han Z, Christianson DW, Kuzma NN, Dmochowski IJ. Cryptophane xenon-129 nuclear magnetic resonance biosensors targeting human carbonic anhydrase. J. Am. Chem. Soc. 2009; 131(2): 563–569.
3. Spence MM, Rubin SM, Dimitrov IE, Ruiz EJ, Wemmer DE, Pines A, Yao SQ, Tian F, Schultz PG. Functionalized xenon as a biosensor. Proc. Natl. Acad. Sci. U. S. A. 2001; 98(19): 10 654–10 657.
4. Spence MM, Ruiz EJ, Rubin SM, Lowery TJ, Winssinger N, Schultz PG, Wemmer DE, Pines A. Development of a functionalized xenon biosensor. J. Am. Chem. Soc. 2004; 126(46): 15 287–15 294.
5. Schröder L, Lowery TJ, Hilty C, Wemmer DE, Pines A. Molecular imaging using a targeted magnetic resonance hyperpolarized biosensor. Science 2006; 314: 446–449.
6. Shapiro MG, Ramirez RM, Sperling LJ, Sun G, Sun J, Pines A, Schaffer DV, Bajaj VS. Genetically encoded reporters for hyperpolarized xenon magnetic resonance imaging. Nat. Chem. 2014; 6: 626–634.
7. Wolber J, Rowland IJ, Leach MO, Bifone A. Perfluorocarbon emulsions as intravenous delivery media for hyperpolarized xenon. Magn. Reson. Med. 1999; 41(3): 442–449.
8. Stevens TK, Ramirez RM, Pines A. Nanoemulsion contrast agents with sub-picomolar sensitivity for xenon NMR. J. Am. Chem. Soc. 2013; 135(26): 9576–9579.
9. Bai Y, Wang Y, Goulian M, Driks A, Dmochowski IJ. Bacterial spore detection and analysis using hyperpolarized 129-Xe chemical exchange saturation transfer (Hyper-CEST) NMR. Chem. Sci. 2014; 5: 3197–3203.
10. Kunth M, Döpfert J, Witte C, Rossella F, Schröder L. Optimized use of reversible binding for fast and selective NMR localization of caged xenon. Angew. Chem. Int. Ed. 2012; 51(33): 8217–8220.
11. Klippel S, Döpfert J, Jayapaul J, Kunth M, Rossella F, Schnurr M, Witte C, Freund C, Schröder L. Cell tracking with caged xenon: Using cryptophanes as MRI reporters upon cellular internalization. Angew. Chem. Int. Ed. 2014; 53(2): 493–496.
12. Rose HM, Witte C, Rossella F, Klippel S, Freund C, Schröder L. Development of an antibody-based, modular biosensor for 129-Xe NMR molecular imaging of cells at nanomolar concentrations. Proc. Natl. Acad. Sci. U. S. A. 2014; 111(32): 11 697–11 702.
13. Schnurr M, Witte C, Schröder L. Functionalized 129-Xe as a potential biosensor for membrane fluidity. Phys. Chem. Chem. Phys. 2013; 15: 14 178–14 181.
14. Zaiss M, Bachert P. Exchange-dependent relaxation in the rotating frame for slow and intermediate exchange – modeling off-resonant spin-lock and chemical exchange saturation transfer. NMR Biomed. 2013; 26: 507–518.
15. Jin T, Kim SG. Advantages of chemical exchange-sensitive spin-lock (CESL) over chemical exchange saturation transfer (CEST) for hydroxyl– and amine–water proton exchange studies. NMR Biomed. 2014; 27: 1313–1324.
16. Zaiss M, Xu J, Goerke S, Khan IS, Singer RJ, Gore JC, Gochberg DF, Bachert P. Inverse *Z*-spectrum analysis for spillover-, MT-, and T1-corrected steady-state pulsed CEST-MRI – application to pH-weighted MRI of acute stroke. NMR Biomed. 2014; 27: 240–252.
17. Zaiss M, Zu Z, Xu J, Schuenke P, Gochberg DF, Gore JC, Ladd ME, Bachert P. A combined analytical solution for chemical exchange saturation transfer and semi-solid magnetization transfer. NMR Biomed. 2015; 28: 217–230.
18. Roeloffs V, Meyer C, Bachert P, Zaiss M. Towards quantification of pulsed spinlock and CEST at clinical MR scanners: an analytical interleaved saturation–relaxation (ISAR) approach. NMR Biomed. 2015; 28: 40–53.
19. McConnell HM. Reaction rates by nuclear magnetic resonance. J. Chem. Phys. 1958; 28: 430–431.
20. Woessner DE. Nuclear transfer effects in nuclear magnetic resonance pulse experiments. J. Chem. Phys. 1961; 35(1): 41–48.
21. Zaiss M, Schnurr M, Bachert P. Analytical solution for the depolarization of hyperpolarized nuclei by chemical exchange saturation transfer between free and encapsulated xenon (HyperCEST). J. Chem. Phys. 2012; 136(14): 144 106.
22. Kunth M, Witte C, Schröder L. Quantitative chemical exchange saturation transfer with hyperpolarized nuclei (qHyper-CEST): Sensing xenon-host exchange dynamics and binding affinities by NMR. J. Chem. Phys. 2014; 141(19): 194 202.
23. Zaiss M, Bachert P. Chemical exchange saturation transfer (CEST) and MR *Z*-spectroscopy in vivo: a review of theoretical approaches and methods. Phys. Med. Biol. 2013; 58(22): R221.
24. Sun PZ. Simplified quantification of labile proton concentration-weighted chemical exchange rate (k_{ws}) with RF saturation time dependent ratiometric analysis (QUESTRA): Normalization of relaxation and RF irradiation spillover effects for improved quantitative chemical exchange saturation transfer (CEST) MRI. Magn. Reson. Med. 2012; 67: 936–942.
25. Meldrum T, Bajaj VS, Wemmer DE, Pines A. Band-selective chemical exchange saturation transfer imaging with hyperpolarized xenon-based molecular sensors. J. Magn. Reson. 2011; 213(1): 14–21.
26. Sun PZ, Wang E, Cheung JS, Zhang X, Benner T, Sorensen AG. Simulation and optimization of pulsed radio frequency irradiation scheme for chemical exchange saturation transfer (CEST) MRI–demonstration of pH-weighted pulsed-amide proton CEST MRI in an animal model of acute cerebral ischemia. Magn. Reson. Med. 2011; 66(4): 1042–1048.
27. Zu Z, Li K, Janve VA, Does MD, Gochberg DF. Optimizing pulsed-chemical exchange saturation transfer imaging sequences. Magn. Reson. Med. 2011; 66(4): 1100–1108.
28. Rancan G, Nguyen T, Glaser S. Gradient ascent pulse engineering for rapid exchange saturation transfer. J. Magn. Reson. 2015; 252C: 1–9.
29. Li AX, Hudson RH, Barrett JW, Jones CK, Pasternak SH, Bartha R. Four-pool modeling of proton exchange processes in biological systems in the presence of MRI-paramagnetic chemical exchange saturation

transfer (PARACEST) agents. Magn. Reson. Med. 2008; 60(5): 1197–1206.
30. Sun PZ. Simplified and scalable numerical solution for describing multi-pool chemical exchange saturation transfer (CEST) MRI contrast. J. Magn. Reson. 2010; 205(2): 235–241.
31. Witte C, Kunth M, Döpfert J, Rossella F, Schröder L. Hyperpolarized xenon for NMR and MRI applications. J. Vis. Exp. 2012; 67: e4268.
32. Witte C, Kunth M, Rossella F, Schröder L. Observing and preventing rubidium runaway in a direct-infusion xenon-spin hyperpolarizer optimized for high-resolution Hyper-CEST (chemical exchange saturation transfer using hyperpolarized nuclei) NMR. J. Chem. Phys. 2014; 140(8): 084 203.

SUPPORTING INFORMATION

Additional supporting information may be found in the online version of this article at the publisher's web-site.